Available online at www.sciencedirect.com
ScienceDirect
Journal of Catalysis 247 (2007) 86–100
JOURNAL OF CATALYSIS
www.elsevier.com/locate/jcat

Epoxidation of propylene with nitrous oxide on Rb_2SO_4-modified iron oxide on silica catalysts

Bart Moens [a], Hendrik De Winne [a], Steven Corthals [a], Hilde Poelman [b], Roger De Gryse [b], Vera Meynen [c], Pegie Cool [c], Bert F. Sels [a,*], Pierre A. Jacobs [a,*]

[a] *Center for Surface Chemistry and Catalysis, Katholieke Universiteit Leuven, Kasteelpark Arenberg 23, B-3001 Heverlee, Belgium*
[b] *Surface Physics and Thin Film Division, Ghent University, Krijgslaan 281-S1, B-9000 Ghent, Belgium*
[c] *Laboratory of Adsorption and Catalysis, Department of Chemistry, University of Antwerp, Universiteitsplein 1, B-2610 Wilrijk, Belgium*

Received 1 November 2006; revised 31 December 2006; accepted 2 January 2007

Available online 20 February 2007

Abstract

The catalytic activity of alkaline and earth alkaline-modified silica-supported metal oxide was investigated for epoxidizing propylene with nitrous oxide. Iron oxide gave the best results, and surprisingly chromium oxide also produced propylene oxide (PO). Unmodified iron oxide catalyst showed low oxidation activity and produced propanal (57% selectivity) in concert with small amounts of acrolein, allyl alcohol, and acetone. After modification, the oxidation rate increased significantly, with PO the principal product. PO selectivities up to 85–90% and space–time yields of 0.25–0.53 mmol PO g^{-1} h^{-1} were obtained over supported iron oxide modified with Rb_2SO_4. A high throughput composition study revealed that other alkali and earth alkali salts were less effective modifiers. Isopropanol decomposition demonstrated that Rb_2SO_4 severely reduced the acidity of the catalyst. As a result of the neutralization, PO isomerization was drastically reduced. Accordingly, when feeding PO instead of propylene with N_2O over the catalyst, a similar reduction of consecutive PO reactions was observed on Rb_2SO_4 modification. Despite the excellent epoxidation results, a catalytic process remains infeasible due to the restricted service time of the catalyst. Thermogravimetric analyses of a spent catalyst showed carbonaceous residues, suggesting that cokes deactivate the catalyst. Feeding PO indicates that PO itself is a source of cokes. Catalyst regeneration is possible without significant loss of performance. UV–vis DRS and EPR were used to determine the local environment of Fe^{3+} in the (un)promoted iron oxide catalyst; the findings suggest well-dispersed distorted tetrahedral Fe^{3+} sites for epoxidation activity. Fe dispersion is ruled by the promoter salts, with both anions and cations being essential. Along with the structural influences, inspection of the catalytic data in concert with XPS and Raman analyses provides evidence of a direct (electronic) promoter effect on the catalytic activity.

Keywords: Partial oxidation; Nitrous oxide; Propylene epoxidation; Iron oxide; Promoter effects; Physicochemical characterization

1. Introduction

Catalytic oxidation preferably uses molecular oxygen as an oxidant. Instead of partial oxidation, the high reactivity of the surface activated oxygen species generated from O_2 often leads to consecutive oxidation and, consequently, to a loss in selectivity. In the last decade, much attention has been given to the use of mild oxidants, such as nitrous oxide (N_2O). N_2O is a gas with a high greenhouse warming potential [1]. Because N_2O is produced abundantly in industry [2], its use as an oxidant offers a promising solution to the environmental problems associated with this gas.

Selective oxidation with N_2O has been demonstrated for benzene [3–19] and methane [19–23] hydroxylation, and for alkane oxidative dehydrogenation over Fe-ZSM-5, and to a lesser extent over ZSM-5 exchanged with other ions [24–29]. Although hydroxylation has first been associated with zeolite framework acidity, N_2O is activated at a metal site, leading to N_2 and atomically adsorbed oxygen, sometimes referred to as α-oxygen [19]. The active O further oxidizes CH_4 and benzene to precursors of methanol and phenol, respectively. Phenol desorbs at reaction temperature [19] and thus is produced catalyti-

* Corresponding authors. Fax: +32 16 32 1998.
E-mail addresses: bert.sels@biw.kuleuven.be (B.F. Sels), pierre.jacobs@biw.kuleuven.be (P.A. Jacobs).

0021-9517/$ – see front matter
doi:10.1016/j.jcat.2007.01.001

cally, whereas the methoxy intermediate decomposes into CO_x and water. Methanol is obtained only after hydrolysis at low temperature [20,30]. Whereas the synthesis of phenol tested at Solutia's demonstration plant [31] points to an economically feasible process, purification of industrial N_2O and catalyst deactivation seem to be an obstacle. In contrast to hydroxylation, the oxidative dehydrogenation mechanism is unclear. Whereas α-sites likely control hydroxylation, either alcohol dehydrogenation or direct oxidative dehydrogenation is expected to occur [25].

Recently, epoxidation of propylene with N_2O has been discussed [32–37]. Because current PO manufacturing suffers from serious drawbacks [38], it is worthwhile to search for new PO routes. The chlorohydrin route faces environmental pollution problems due to quantitative $CaCl_2$ production, whereas the hydroperoxide process is handicapped due to its dependence on the market price of the alcohol byproduct. Propylene epoxidation with N_2O may provide an environmentally benign PO production route as no byproducts are formed:

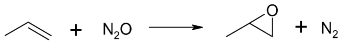

Iron oxide loaded on silica has been proposed for the selective epoxidation with N_2O [32–37]. All authors agree on the necessity of alkali-promoted iron oxide. After modification with sodium acetate, a PO yield and selectivity of 4.8 and 40% were obtained. Almost no PO was formed over unpromoted silica-supported iron oxide [36,37]. Cesium acetate was advanced as the preferred additive, providing PO yields of 7.5% with 75% PO selectivity at 650 K [32]. KCl was presented as a superior modifier for iron oxide supported on structured mesoporous silica, such as SBA-15 and MCM-41, as well as on steam-treated ZSM-5 [33–35]. A change in redox behavior of the iron catalyst was observed as a result of the KCl promotion [34]. In addition, on modification with alkali metal salts, a dramatic shift in oxidation mechanism, from allylic oxidation for unpromoted catalysts to epoxidation for promoted catalysts, was proposed [33,34]. A PO selectivity of 80% at 4% propylene conversion was reported.

So far, only iron oxide and a few promoters have been studied. To gain a broader view of the potential of various metal oxides, we have systematically investigated the catalytic performance of a series of supported metal oxides modified with various alkaline and earth alkaline additives. For practical reasons, we have chosen to synthesize the catalyst via a single impregnation step of the two constituents, that is, metal and promoter salt.

High-throughput screening provided us with a unique catalyst composition consisting of iron oxide supported on silica modified with Rb_2SO_4. Having determined an optimal formulation, this paper attempts to correlate the catalytic features (activity/selectivity) of the catalyst with its surface acid–base properties and structural/electronic properties. A reaction mechanism of the iron-catalyzed epoxidation is proposed based on a comparison of the products formed in a typical propylene epoxidation process with the results of PO co-feeding experiments in reaction conditions.

2. Experimental

2.1. Catalyst preparation

Catalysts were prepared by incipient wetness impregnation with a fresh aqueous solution of a metal chloride (or nitrate) precursor (e.g., $FeCl_2$ for iron oxide) together with the promoter salt on commercial silica (Silica Kieselgel 60, Fluka; specific surface area, 500 $m^2\,g^{-1}$; pore volume, 0.75 $ml\,g^{-1}$; average pore diameter, 40–63 nm). Concentrations of the aqueous salt solutions typically range between 9 and 180 mM in $FeCl_2$ and 0.15 and 4.83 M in promoter salt. After impregnation, the catalyst is dried for 3 h at 373 K and calcined in air at 973 K for 6 h.

2.2. Catalyst testing

Epoxidation was studied using 4 parallel fixed-bed flow quartz reactors (3 mm i.d.) operating at atmospheric pressure and 683 K. Each reactor tube contained 0.10 g catalyst pellets ranging in diameter from 125 to 250 μm. N_2O (purity 99.5%) and O_2 (purity 99.5%) were used as oxidants. After pretreatment of the catalyst at 793 K in O_2 atmosphere for 3 h, the reaction was started by introducing a mixture of propylene and N_2O in He at reaction temperature. The gas rates were regulated using electronic thermal mass flow controllers. A molar ratio of C_3/N_2O/He (1/5/30) was used with a total flow rate equivalent to 7.5 $ml\,min^{-1}$ per reactor tube (GHSV [STP] = 4.5 $L\,h^{-1}\,g^{-1}$). The outlet gases were analyzed via on-line GC analysis using a Poraplot Q column connected to an internal methanator and a FID. All connections and valves between the reactor tube and the gas chromatograph were heated at about 423 K to prevent condensation. The results after 180 min are presented and used for discussion, unless stated otherwise, despite the imperfect steady-state conditions due to catalyst deactivation (vide infra). Co-feeding of PO was carried out using 2.5 vol% PO in Ar.

2.3. Catalyst characterization

Isopropanol decomposition using temperature ranging from 523 to 573 K was studied with 0.10 g of sample and a flow of 7.5 $ml\,min^{-1}$ consisting of 4.2 kPa isopropanol in He. Acetone and propylene were analyzed with on-line gas chromatography with a FID such as for the oxidation experiments.

Thermogravimetric tests were done in a TGA Q500 apparatus (TA Instruments) on samples discharged from the reactor after several hours on stream. The tests were made in a flow of 90 $ml\,min^{-1}$ O_2, which passes tangentially to the pan of the TGA apparatus containing approximately 25 mg of sample. The heating rate was 5 K/min from 303 to 1073 K. The samples turned from black to white after the TGA experiments, indicating complete C removal.

XRD measurements were carried out to study the eventual formation of crystalline phases in the catalyst; a STOE STADI P transmission diffractometer was used with Cu$K\alpha$ radiation

($\nu = 1.54$ Å) measuring between 5 and 60 degrees 2θ, with 2.5 degrees per step analyzing 500 seconds per step.

Surface analysis was performed by XPS using a Perkin Elmer PHI ESCA 5500 electron energy analyzer system combined with monochromatic 450 W Al$K\alpha$ X-ray radiation. Wide scan surveys and high-resolution multiplexes were performed at constant pass energies of 187.85 and 23.5 eV, respectively. Samples were fixed in an indium foil to avoid contamination of the carbon signals.

FT-Raman spectra were recorded on a Nicolet Nexus FT-Raman spectrometer with a Ge detector and a 1064 nm Nd:YAG laser. Samples were measured in a 180° reflective sampling configuration. A total of 4000 scans were averaged for each sample, with a resolution of 8 cm^{-1}. The laser power was set between 1.0 and 2.0 W. The samples that showed heating effects (broad band around 3000 cm^{-1} Raman shift) were measured at laser powers of 1 W maximum.

Diffuse reflectance UV–vis spectra were obtained on a Varian Cary 5 spectrophotometer equipped with a diffuse–reflectance accessory. Spectra were measured in the reflectance mode (R_∞) and converted according to the Kubelka–Munk function $F(R_\infty)$. The spectra of the samples calcined in dry air at 793 K were collected between 200 and 2500 nm with $BaSO_4$ as a reference.

EPR measurements were carried out with a cw X-band Bruker ESP 300E instrument (microwave frequency ≈ 9.5 GHz) equipped with a rectangular TE104 cavity. EPR spectra were measured using a field modulation amplitude of 3.2 mT, a modulation frequency of 100 kHz, and microwave power of 0.1–0.2 mW. EPR spectra of samples calcined in dry air at 793 K were recorded at 120 K and at room temperature.

3. Results

3.1. Catalytic properties of various promoted silica-supported iron oxide catalysts

The catalytic performances at 683 K of promoted FeO_x/silica for propylene oxidation are summarized in Table 1. Under the specified conditions, no reaction occurred over a reactor tube filled with glass wool (entry 1). The silica support was slightly active, although conversion was low (entry 2). The modest activity is likely attributed to iron impurities (<100 ppm wt%). When 0.1 wt% iron was introduced in the silica, oxidation was in agreement with earlier observations (entry 3) [32–37], underlining the active role of iron. Despite its oxidation ability, unpromoted FeO_x/silica showed a PO selectivity of <1% at a propylene conversion of 2.6% (entry 3), with propanal (PA) the main product formed with 57% selectivity. Lower amounts of acrolein (ACR), allylic alcohol (AA), and acetone (AC) were also found.

Other data in Table 1 (entries 4–10) demonstrate that modifying the iron catalyst with acetate salts clearly produced PO from propylene. Screening tests with various alkali (Li, Na, K, Rb, and Cs) and earth alkali (Mg and Ba) acetate salts revealed that univalent cations were generally better promoters than bivalent cations (entries 5 and 9).

Table 1
Effect of alkali and earth alkali acetate modification of FeO_x on silica on the epoxidation of propylene with N_2O

Entry	Active element/ promoter/support	C_3 conv. (%)	Selectivity (%)							
			PO	ACR	PA	AC	AA	CO	CO_2	Other
1	–/–/–	0	0	0	0	0	0	0	0	0
2	–/–/SiO_2	0.8	0	18	57	0	13	0	6	6
3	Fe/–/SiO_2	2.6	1	13	57	1	7	1	7	13
4	Fe/Li/SiO_2	5.1	16	16	16	3	15	6	20	8
5	Fe/Na/SiO_2	7.3	26	10	9	9	2	6	30	8
6	Fe/K/SiO_2	6.5	22	5	3	1	1	11	48	9
7	Fe/Rb/SiO_2	3.9	9	2	0	0	0	9	70	10
8	Fe/Cs/SiO_2	3.1	2	0	0	2	0	15	78	3
9	Fe/Mg/SiO_2	3.5	0	12	53	1	7	4	7	16
10	Fe/Ba/SiO_2	4.5	6	14	24	3	15	4	13	21

Notes. 1. Reaction parameters: $C_3/N_2O/He = 1/5/30$; GHSV = 4.5 L h^{-1} g^{-1}; partial pressure of propylene and N_2O is 2.8 and 13.9 kPa, respectively; T = 683 K; TOS = 180 min.
2. Catalyst: Fe 0.1 wt%; promoter/Fe = 36 (mol/mol).
3. PO = propylene oxide, ACR = acrolein, PA = propanal, AC = acetone, AA = allylic alcohol, other = cracking products (CH_4, C_2H_4, C_2H_6 + their oxygenated species).

For a series of monovalent alkali metal acetates, activities and PO selectivities/yields showed the following sequence (see Supplementary material, Fig. S1): Na > K > Li > Rb > Cs. This order emphasizes that Na is the modifier of choice among the alkali metal acetates.

Among the Na acetate-promoted oxides of other potentially active elements originating from the chloride and nitrate salts of Zn, Mn, Co, Ru, Cu, Ni, Au, Rh, Cr, Sm, Eu, La, Nd, and Ag, with a metal loading between 0.1 and 0.2 wt%, only chromium oxide (from $CrCl_3$ impregnation) was capable of producing PO. A PO selectivity of approximately 10% at 0.5% conversion was achieved. This low but distinct PO yield is worth mentioning, although not understood. Indeed, to the best of our knowledge, chromium oxide has never before been associated with selective epoxidation processes.

Various support materials for Na acetate-promoted iron oxide, including ZSM-5, Al_2O_3, TiO_2, $CaCO_3$, $BaCO_3$, and amorphous SiO_2/Al_2O_3 with varying Si/Al ratios, were used as well. None showed activity for the selective (ep)oxidation of propylene with N_2O; only CO_x was formed. With the carbonate supports, the system failed to show any oxidation activity at all.

The Na acetate-promoted iron oxide on silica, showing superior PO formation yields with N_2O, also failed to show any epoxidation selectivity with O_2 as oxidant. Mainly CO_2 was formed, along with small amounts of acrolein and acetaldehyde.

Finally, the alkali metal acetate promoter salts were substituted for the corresponding nitrates (data not shown) and sulfates (Table 2). Surprisingly, on modification with Rb_2SO_4, the catalyst showed a PO selectivity of 76% at 9.1% conversion, corresponding to a PO formation rate of 0.37 mmol g^{-1} h^{-1} (Table 2, entry 3). This result is clearly better than that obtained with Na acetate (0.10 mmol g^{-1} h^{-1} PO formation rate; Table 1, entry 5). Modification of the iron catalyst with a series of sulfate salts (Table 2) yielded the following epoxidation activity sequence: Rb ⩾ Cs > K > Tl > Na > VO. Rb and Cs sulfate promoted the PO yield up to values of 5–6%. The different

Table 2
Propylene conversion and product selectivities using sulfate salts as promoter for FeO_x on silica

Entry	Active element/ promoter/support	C_3 conv. (%)	Selectivity (%)							
			PO	ACR	PA	AC	AA	CO	CO_2	Other
1	$Fe/Na_2SO_4/SiO_2$	1.5	73	0	0	0	0	0	24	3
2	$Fe/K_2SO_4/SiO_2$	3.0	90	0	0	0	0	0	10	0
3	$Fe/Rb_2SO_4/SiO_2$	9.1	76	0	2	2	0	0	11	9
4	$Fe/Rb_2SO_4/SiO_2$[a]	8.5	76	0	3	2	0	0	12	7
5	$Fe/Cs_2SO_4/SiO_2$	6.9	67	0	8	1	0	2	12	10
6	$Fe/VO(SO_4)/SiO_2$	0.3	0	0	0	0	0	0	100	0
7	$Fe/Tl_2SO_4/SiO_2$	2.8	68	0	10	0	0	0	15	7

Notes. 1. Reaction parameters: $C_3/N_2O/He = 1/5/30$; GHSV $= 4.5\,L\,h^{-1}\,g^{-1}$; partial pressure of propylene and N_2O is 2.8 and 13.9 kPa, respectively; $T = 683$ K; TOS = 180 min.
2. Catalyst: Fe 0.1 wt%; promoter cation/Fe = 9 (mol/mol).
[a] Second run after regeneration of the catalyst by burning the cokes in air.

Table 3
Influence of promoter anion and anion concentration on the catalytic performance of 0.1 wt% FeO_x on silica in the epoxidation of propylene with N_2O

Entry	Active element/ promoter/support	Rb/Fe	C_3 conv. (%)	Selectivity (%)							
				PO	ACR	PA	AC	AA	CO	CO_2	Other
1	$Fe/RbCl/SiO_2$	36	1.9	3	0	0	0	0	22	75	0
2	$Fe/RbOH/SiO_2$	36	1.7	6	0	0	0	0	18	76	0
3	$Fe/RbF/SiO_2$	36	2.2	5	0	0	0	0	19	76	0
4	$Fe/Rb_2CO_3/SiO_2$	36	2.3	0	0	0	0	0	19	81	0
5	$Fe/Rb_2SO_4/SiO_2$	2.3	3.2	62	0	0	0	0	7	8	23
6	$Fe/Rb_2SO_4/SiO_2$	4.5	2.3	91	0	1	0	0	0	7	1
7	$Fe/Rb_2SO_4/SiO_2$	9	9.1	76	0	2	2	0	0	11	9
8	$Fe/Rb_2SO_4/SiO_2$	18	6.1	82	0	2	1	0	0	10	5
9	$Fe/Rb_2SO_4/SiO_2$	36	7.3	66	2	4	4	2	2	12	8

Notes. 1. Reaction parameters: $C_3/N_2O/He = 1/5/30$; GHSV $= 4.5\,L\,h^{-1}\,g^{-1}$; partial pressure of propylene and N_2O is 2.8 and 13.9 kPa, respectively; $T = 683$ K; TOS = 180 min.
2. Catalyst: Fe 0.1 wt%; promoter cation/Fe = 36 (mol/mol).

sequences for the alkali metal acetates and sulfates and combination of Rb with other anions (Table 3, entries 1–4), suggest that both cation and anion play roles as activity/selectivity-enhancing promoters. To the best of our knowledge, the superior properties of Rb_2SO_4-promoted iron oxide on silica as catalyst in the epoxidation of propylene with N_2O have not been reported before.

The effect of an increased Fe loading of the catalyst at constant atomic Si/Rb ratio of 50 is shown in Fig. 1. A sharp maximum in the PO yield curve is seen for an iron content of 0.15 wt%, corresponding to an average Fe surface density of 0.032 Fe atoms per nm^2 and a PO formation rate of 0.49 mmol PO $g^{-1}\,h^{-1}$. The activity per iron site remained around 18 mmol PO $mmol^{-1}$ Fe h^{-1}, much higher than the published values (~5 mmol PO $mmol^{-1}$ Fe h^{-1} [33–35]). The dependence of activity on iron surface density supports the concept that the degree of dispersion of the iron species on the surface of SiO_2 contributes to the epoxidation properties of the catalyst. Despite the slight revival of oxidation activity at iron loadings >0.6 wt% Fe, PO yields decreased gradually with increasing Fe content. Fe_2O_3 and $Fe_2(CO_3)_3$ showed negligible epoxidation activity. The overall parallel changes of propylene conversion and PO yield curves, at least between 0.05 and 0.6 wt% Fe loading (i.e., between 0.011 and 0.13 Fe atoms per nm^2) indicate that PO selectivities remained almost unchanged between 60 and 75%.

The influence of Rb/Fe molar ratio was investigated for 0.1 wt% iron catalyst (Table 3, entries 5–9). For Rb/Fe ratios of 2.3–36, propylene conversion clearly showed an optimum of 9% for an Rb/Fe ratio of 9, resulting in a PO yield of 7%, corresponding to a PO formation rate of 0.37 mmol $g^{-1}\,h^{-1}$. A similar exercise was carried out for the catalyst with 0.15 wt% iron. A conversion of 13% for a Rb/Fe molar ratio of 12 was found, resulting in an optimal PO yield of 8.1% and a PO formation rate of 0.44 mmol $g^{-1}\,h^{-1}$. In summary, these results

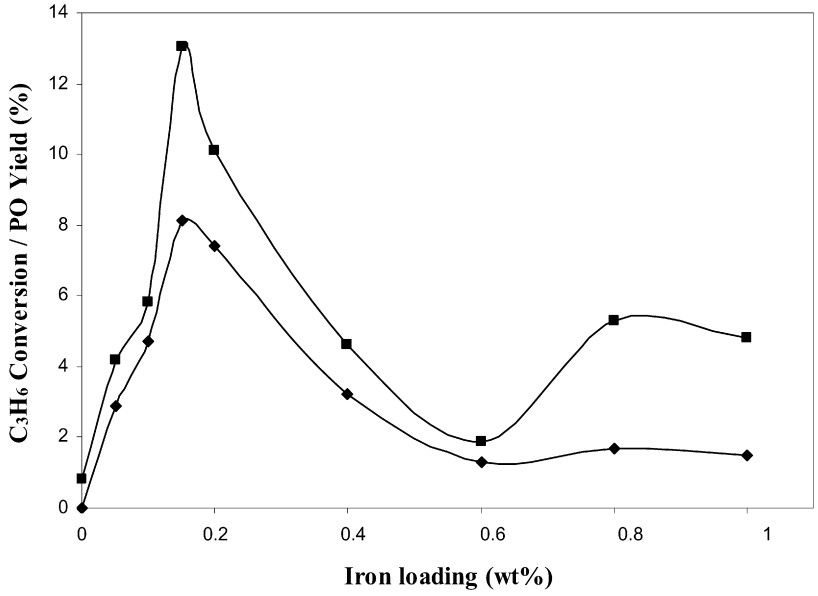

Fig. 1. Effect of iron loading on catalytic performance of Rb sulfate-modified FeO_x on silica in the epoxidation of propylene with N_2O. Reaction parameters: $C_3/N_2O/He = 1/5/30$; GHSV $= 4.5\,L\,h^{-1}\,g^{-1}$, $T = 683$ K, TOS = 180 min. Catalyst: Si/Rb = 50 (mol/mol). (■) C_3H_6 conversion, (◆) PO yield.

Table 4
Influence of reaction temperature on the catalytic performance of Rb_2SO_4-modified FeO_x supported on silica[a] in the epoxidation of propylene with N_2O

Entry	Temp. (K)	C_3 conv. (%)	Selectivity (%)							
			PO	ACR	PA	AC	AA	CO	CO_2	Other
1	598	0.9	88	0	0	0	0	2	10	0
2	623	2.3	85	0	1	1	0	3	9	1
3	653	7.2	71	0	3	2	1	6	9	8
4	683	13	62	0	4	7	2	9	8	8
5	693	15.7	56	0	4	2	2	11	10	15

Note. Reaction parameters: $C_3/N_2O/He = 1/5/30$; GHSV $= 4.5\,L\,h^{-1}\,g^{-1}$; partial pressure of propylene and N_2O is 2.8 and 13.9 kPa, respectively; TOS = 180 min.
[a] Catalyst: Fe 0.15 wt%; Rb/Fe = 12 (mol/mol).

suggest that an optimum molar Rb/Fe ratio of approximately 10 is needed. Higher Rb concentrations have only a minor effect on the PO yield, whereas lower Rb concentrations are clearly detrimental.

The effect of reaction temperature was investigated in the range of 598–693 K (Table 4). At increasing temperatures, the selectivity for PA, AC, AA, CO, and other unidentified products gradually increased at the expense of PO, whereas CO_2 selectivity did not change with temperature. CO_2 seems to be formed independently from PO due to reactive lattice oxygen. An Arrhenius plot of the experimental data in Table 4 provides the apparent activation energy (79.8 kJ mol^{-1}) for the Rb_2SO_4-promoted 0.15 wt% Fe on silica, indicating the absence of mass transfer limitations.

3.2. Stability in time of catalytic performances during epoxidation of propylene

The catalytic behavior of a 0.15 wt% Fe on silica catalyst modified with Rb_2SO_4 (Rb/Fe = 12) with time on stream is shown in Fig. 2. The conversion of propylene gradually decreased from nearly 17% after 80 min to 8% after 360 min of reaction under the conditions shown in the figure. The highest PO yield measured in this study (9.9%) was obtained after 80 min and corresponds to a PO formation rate of 0.53 mmol PO $g^{-1}\,h^{-1}$. The PO selectivity gradually increased from 59 to 66% in the same time span. Similar observations have been reported for benzene hydroxylation and alkane oxidative dehydrogenation with N_2O [3–19,24–29]. The rapid decline of catalytic activity has been attributed to coke formation blocking the active sites.

A closer look at the spent catalyst showed a black coloration of the initially white catalyst after 7 h on stream. Thermogravimetric analysis of the black residue (Fig. 3, insert) showed an initial low-temperature weight loss associated with water removal; a second change at 673–873 K, with a maximum in the derivative curve at about 805 K, corresponds to a further weight loss of 3.5%, indicating combustion of carbonaceous deposits.

The correlation curve between the actual PO yield and the accumulated PO production (Fig. 3) yields information on catalyst deactivation. The slope of the curve is a measure of deactivation rate, whereas the x- and y-intercepts are indicative of the theoretical PO production capacity of the catalyst and the theoretical maximum PO yield per unit amount of catalyst assuming no deactivation, respectively. The 0.15 wt% iron oxide on silica promoted with Rb_2SO_4 (Rb/Fe = 12) was compared with a literature catalyst with a 1 wt% iron oxide on SBA-15 modified with KCl (K/Si = 0.04) [33]. Both catalysts clearly show deactivation, and thus a limited catalyst service time; moreover, the Rb_2SO_4-modified catalyst shows a higher potential for PO production.

After calcining the spent catalyst in O_2 at 823 K, the activity of the Rb_2SO_4-modified FeO_x/silica was almost fully restored, as can be derived from the data in Table 2 (entries 3 and 4).

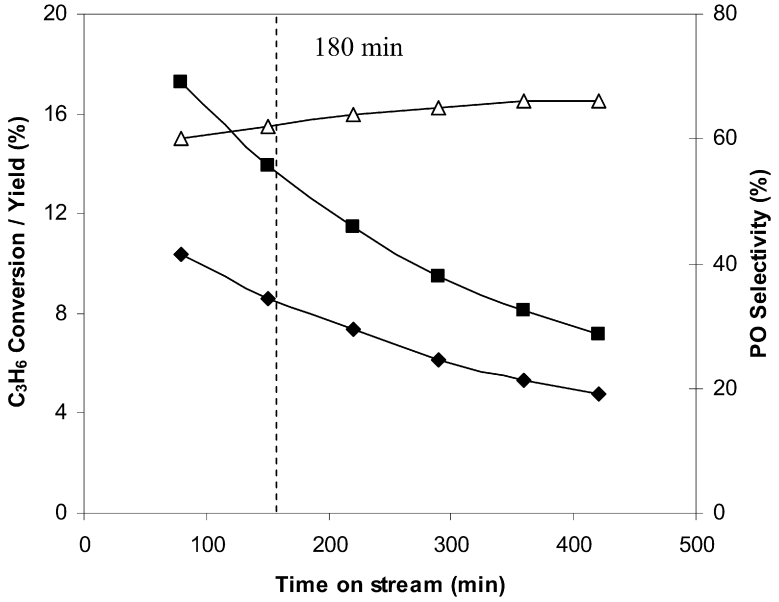

Fig. 2. Catalytic behavior of Rb_2SO_4-modified FeO_x supported on silica as function of time-on-stream at 683 K. Reaction parameters: $C_3/N_2O/He = 1/5/30$; GHSV $= 4.5\,L\,h^{-1}\,g^{-1}$. Catalyst: 0.15 wt% Fe; Rb/Fe = 12. (■) C_3H_6 conversion, (△) PO selectivity, (◆) PO yield.

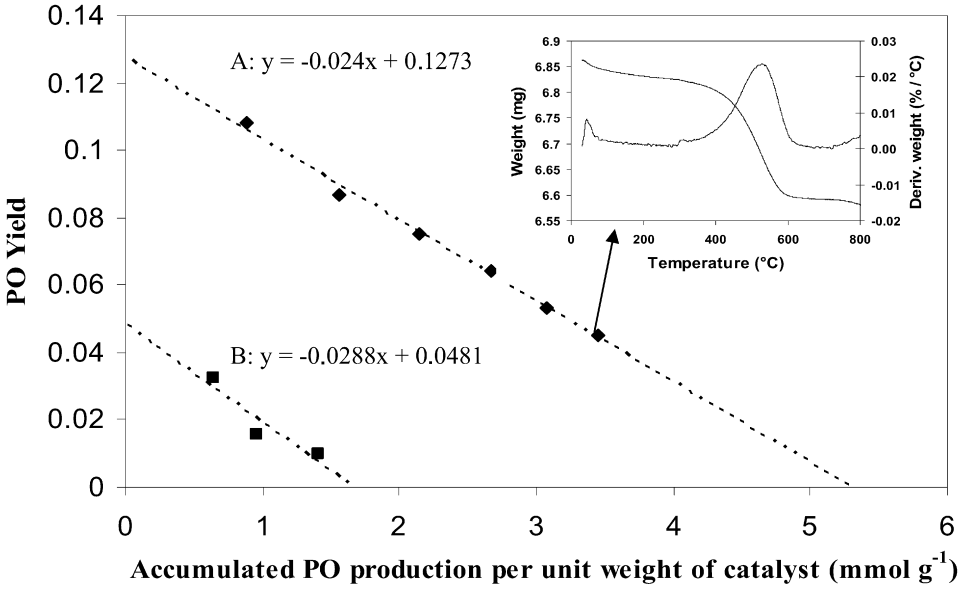

Fig. 3. Correlation between accumulated PO production per weight catalyst and the actual PO yield for modified FeO_x on silica in the epoxidation of propylene with N_2O. Curve A: 0.15 wt% Fe on silica, Rb/Fe = 12; $C_3/N_2O/He$ = 1/5/30; GHSV = 4.5 $L\,h^{-1}\,g^{-1}$, T = 683 K, TOS = 180 min. Curve B: K^+–1 wt% FeO_x/SBA-15 (data obtained from [33]). Insert: thermogravimetric weight and derivative weight loss curves obtained in air flow, for a catalyst discharged after test of Fig. 2 (Rb_2SO_4-modified 0.15 wt% FeO_x on silica with Rb/Fe = 12).

3.3. Mechanistic features: The stability of propylene oxide in reaction conditions

Because propylene does not form coke by interaction with the catalyst in absence of N_2O, the carbonaceous residues probably originate from consecutive transformations of the oxidized products. The origin of PO instability may be associated with isomerization over Lewis or Brönsted acid sites. To rationalize the relationship between catalyst acidity and PO stability, a control experiment with PO feed was carried out (Table 5). In the presence of N_2O, PO showed only slight thermal instability in a reactor loaded with quartz wool. However, in the presence of bare silica, PO instability was dramatically increased (entry 1), resulting in the formation of mainly PA and AA. AA can be further oxidized into ACR. Nearly the same PA selectivity was obtained when 0.1 wt% iron was added to the silica support (entry 2). The AA abundantly formed on the support was now converted into CO_x (mainly CO) and unidentified products. On the other hand, addition of Rb_2SO_4 to the iron catalyst partially restored PO stability (entry 4); only 28.9% of the PO was converted into PA, AC, CO_x, and traces of AA. Thus an important effect of the promoter is the prevention of secondary reactions of PO. Similar observations can be made when comparing the behavior of the promoted and unpromoted catalysts in a propylene reaction (entries 3 and 5). With the unpromoted catalyst, PA rather than PO was the preferred product. Furthermore, black coloration of the catalyst occurred in each case, indicating that PO induced coke.

The PO feeding experiments also provide some elucidation regarding the reaction mechanism. The amount of PO fed in the experiment can be assumed to be formed initially in the epoxidation reaction. Table 5 clearly suggests that initially PO was the primary product, and that PO stability mainly determined the final product distribution. In this way a Rb_2SO_4-promoted catalyst showed excellent PO selectivity, whereas the analogue unpromoted catalyst gave isomerization products.

Table 5
Product selectivities from propylene and PO

Entry	Active element/ promoter/support	Feed	Conv. (%)	Selectivity (%)						
				PO	ACR	PA	AC	AA	CO_x	Other
1	–/–/SiO_2	PO	100	–	6	49	1	28	3	13
2	Fe/–/SiO_2	PO	100	–	10	48	2	6	9	25
3	Fe/–/SiO_2	Propylene	2.6	1	13	57	1	7	8	13
4	Fe/Rb_2SO_4/SiO_2[a]	PO	28.9	–	0	14	30	3	18	35
5	Fe/Rb_2SO_4/SiO_2[a]	Propylene	6.1	82	0	2	1	0	10	5

[a] Catalyst: 0.1 wt% Fe; Rb/Fe = 18 (mol/mol).

3.4. Catalyst characterization

3.4.1. Dehydration of isopropanol

PO instability plays an important role in the propylene reaction with N_2O. Acidity characterization of the catalyst can support observations concerning PO isomerization. The isopropanol (IPA) decomposition is a model reaction for characterizing acid and/or basic properties of the catalyst [39]. Dehydration of IPA to propylene and/or di-isopropyl ether requires Brönsted acid sites, whereas dehydrogenation to acetone occurs on basic (redox) centers. Results of this experiment are listed in Table 6. Silica and 0.1 wt% iron loaded silica at 573 K showed IPA conversions of 9.4 and 14%, respectively (entries 1 and 2). The high propylene selectivities of 98 and 99%, respectively, suggest the presence of strong acidity. In contrast to the results of PO feeding presented in Section 3.3, here the presence of iron clearly influenced IPA conversion; adding iron increased the Brönsted acidity of the catalyst. Promotion with Rb_2SO_4 re-

Table 6
Isopropanol decomposition at 573 K as characterization of acidity

Entry	Active element/ promoter/support	IPA conv. (%)	Selectivity (%)		
			Propylene	Acetone	CO_2
1	–/–/SiO_2	9.4	98	2	0
2[a]	Fe/–/SiO_2	14	99	1	0
3[a]	Fe/Rb_2SO_4/SiO_2	0.6	75	25	0

Note. Reaction parameters: GHSV = 4.5 L h^{-1} g^{-1}; TOS = 30 min.
[a] Catalyst: 0.1 wt% Fe; Rb/Fe = 18 (mol/mol).

sulted in neutralization of almost all acid sites, as evidenced by the low IPA conversion of 0.6% at 573 K (entry 3), in agreement with the mechanistic proposal. Thus, unpromoted iron silica with acid sites only resulted in PO isomerization products, whereas Rb_2SO_4-modified iron silica led to seriously reduced PO isomerization. The proposed mechanism, with PO as main product and acid-catalyzed PO isomerization determining the final product selectivity, is thus supported.

3.4.2. Thermogravimetric analysis

Thermogravimetric analysis (TGA) is a useful tool for studying catalyst synthesis and deactivation. TGA analysis of a used Rb_2SO_4 promoted catalyst is shown in Fig. 3; coke formation was already reported in detail in Section 3.2.

To study catalyst synthesis, a batch of Rb_2SO_4-promoted iron oxide on silica was prepared as stated in Section 2, but was not calcined. Calcination was simulated with the TGA device, and the mass loss was compared to that of pure silica (Fig. 4). The two samples showed the same initial mass loss course: a large weight loss at low temperature (348–373 K) attributed to physisorbed water, followed by a slow weight loss due to loss of chemisorbed water at much higher temperature (623–673 K). However, whereas the mass of silica remained nearly constant from 923 K, the Rb_2SO_4-promoted catalyst started to lose more mass at ∼973 K (= the calcination temperature). We attributed this mass loss to the decomposition of Rb_2SO_4 into basic Rb_2O and SO_3. However, the decomposition was not complete; Raman measurements (vide infra) showed the presence of small amounts of sulfate, which is probably essential for an enhanced activity.

3.4.3. X-ray diffraction

X-ray diffraction was carried out to search for crystallites in the catalyst powder. Fig. 5 shows the results of promoted FeO_x on silica with different amounts of Rb_2SO_4. Three distinct signals could be distinguished: $d = 3.51$ (25.3°), 3.12 (28.6°), and 3.00 (29.7°). The diffraction pattern of the catalyst with Rb/Fe = 4.5, 12, and 18 also shows a small signal at $d = 3.30$ (26.5°). After comparing these signals with a database [40], the signals at $d = 3.12$ and 3.00 are assigned to crystalline Rb_2SO_4; the small signal at $d = 3.3$ to RbCl; and the signal at $d = 3.51$, appearing only at the largest promoter concentrations, to Rb_2O. In conclusion, XRD measurement suggests that the active iron species formed an amorphous phase or well-dispersed crystallites too small to detect, whereas an excess of Rb_2SO_4 led to hexagonal Rb_2SO_4 crystallites.

3.4.4. XPS

XPS was performed to study the surface composition and examine the deposited cokes. Both wide-scan surveys and high-resolution multiplexes per element were performed on unpromoted and Rb_2SO_4-promoted iron oxide on silica (see Supplementary material, Figs. S2–S3). However, the surface densities of Fe and S were too low (atomic concentrations ∼0.2 at%) to allow identification of the exact oxidation valence of both elements on the catalyst surface. Under strict reservation, the binding energy [referenced to Si2p (SiO_2) at 103.4 eV] of 709.8 eV of iron on the Rb_2SO_4-promoted catalyst could be best com-

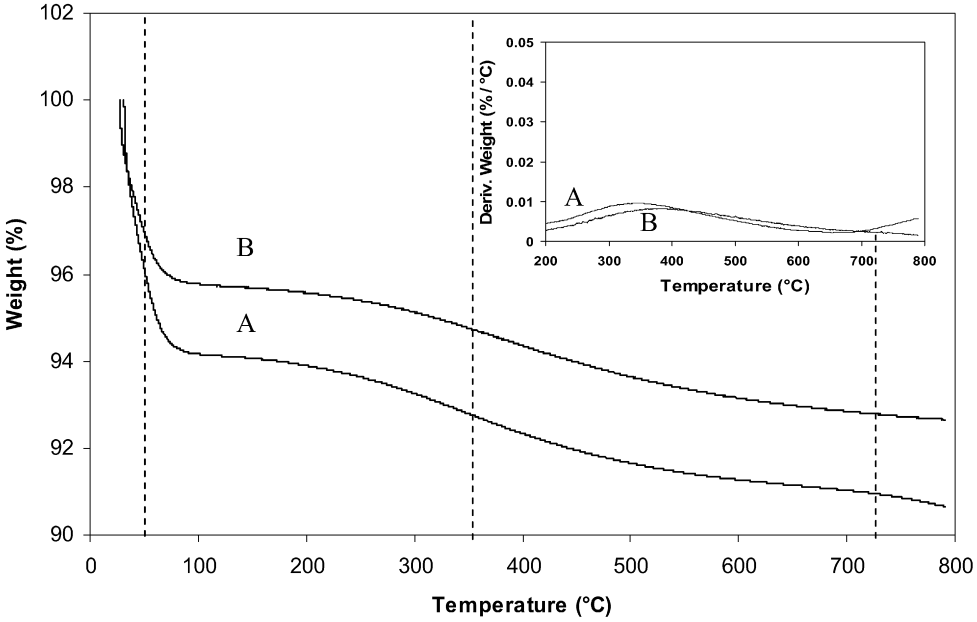

Fig. 4. Thermogravimetric weight and derivative weight loss (insert) curves obtained in air flow, measured for a fresh, uncalcined catalyst (A: Rb_2SO_4-modified 0.15 wt% FeO_x on silica with Rb/Fe = 12) in comparison with blanco silica support (B).

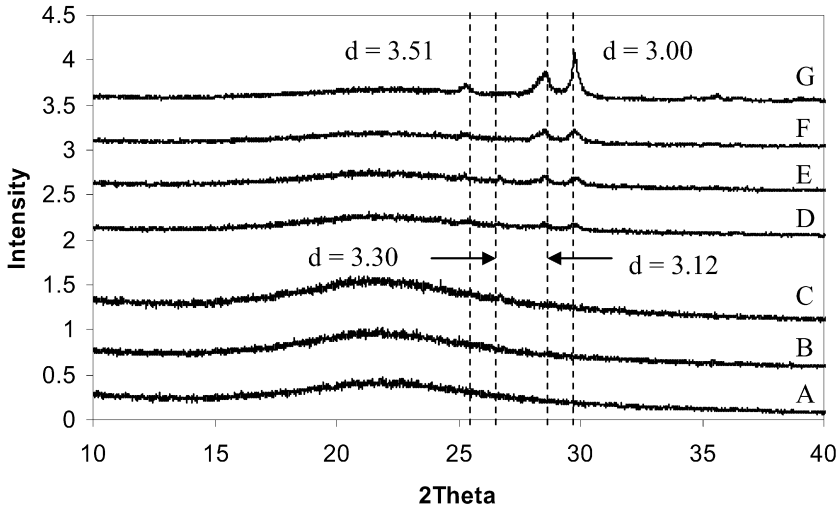

Fig. 5. X-ray diffraction of promoted FeO_x on silica with different amounts of Rb_2SO_4. Catalyst: 0.15 wt% iron; (A) 0, (B) 2.3, (C) 4.5, (D) 12, (E) 18, (F) 36, and (G) 72 Rb/Fe.

pared to that of FeO (709.3–710.2 eV) and Fe_2O_3 (~710.7 eV). Due to the higher atomic mass, Rb was easier to detect; Rb signals were clearly visible according to an atomic Rb concentration of 0.8 at% on the promoted catalyst. No chloride could be detected with XPS.

To analyze the cokes, XPS measurements of fresh and used catalyst were compared (see Supplementary material, Fig. S4). The atomic C concentration clearly rose with the use of this catalyst, while the surface concentrations of other elements remained unchanged. In principle, incorporation of O as carbonyl, alcohol, or ether functions should be visible due to increasing binding energy of the C signals. However, the binding energy of the C signal did not rise as expected (fresh: 284.70 eV, used: 283.78 eV), indicating the presence of oxygen-free C deposits.

3.4.5. Raman spectroscopy

Raman spectroscopy was carried out to search for sulfate on the calcined catalysts and study the optimization of promoter concentration. Catalysts loaded with 0.1 wt% iron and different amounts of Rb_2SO_4 were measured (Fig. 6). Below Rb concentrations of Rb/Fe = 18, no clear signals could be distinguished, except for a small one at 1035 cm^{-1} first appearing at Rb/Fe = 9. This signal did not originate from Rb_2SO_4, but showed a strong resemblance to the ν_s^1 vibration of $Fe_2(SO_4)_3$ appearing at 1035–1045 cm^{-1}. Starting from a concentration of Rb/Fe = 18, five extra signals were detected at 445, 622, 977, 1105, and 1135 cm^{-1}. According to the literature [41,42], these signals can be assigned to the different S–O vibrations of hexagonal Rb_2SO_4: symmetrical stretching ($\nu_s^1 = 977\ cm^{-1}$), asymmetrical stretching ($\nu_s^3 = 1105$ and 1135 cm^{-1}), and bending ($\nu_s^2 = 445$ and $\nu_s^4 = 622\ cm^{-1}$) vibrations. In conclusion, for Rb/Fe < 9, no Rb_2SO_4 could be detected; sulfate remaining after calcination was probably coordinated to iron sites, explaining the signal at 1035 cm^{-1}. Raising the Rb concentration above Rb/Fe = 9 clearly led to crystalline Rb_2SO_4, confirming the XRD results.

3.4.6. UV–vis spectroscopy

UV–vis DRS was carried out to study the coordination and dispersion of the loaded iron. Fig. 7 shows the results of promoted FeO_x on silica with different amounts of iron, ranging from 200 to 600 nm. Absorption in this region is attributed to CT bands from ligand to isolated Fe^{3+} (O → Fe LMCT band, 200–335 nm) and *d–d* transitions (335–590 nm) [43], with the latter covered by a strong tail of the LMCT bands [44]. In the LMCT range, spectra were characterized by four distinct signals: 215–220, 245–250, 275, and 375 nm. According to the literature [43,45–52], the first two signals can be assigned to LMCT transitions ($t_1 \rightarrow t_2$ and $t_1 \rightarrow e$) from isolated iron in tetrahedral coordination, the signal at 275 nm can be assigned to LMCT transition of isolated iron in octahedral coordination, and the signal at 375 nm is usually attributed to octahedral Fe^{3+} in small oligonuclear clusters. The presence of large Fe_2O_3 particles is unlikely, because no LMCT feature above 450 nm is present.

The absorption observed for the silica support (Fig. 7, A), with a band at 220 nm and a shoulder at 245 nm, is due to iron impurities in the silica, attributed to framework Fe^{3+} in tetrahedral coordination. Raising the iron loading to 0.2 wt% iron clearly caused a red shift (to 230 and 260 nm) (Fig. 7, B–E). These bands can also be assigned to tetrahedral Fe, probably located at extra-framework positions with asymmetric or distorted coordination. The appearance of a shoulder at around 275 nm (Fig. 7, E) points to the presence of small amounts of octahedral Fe^{3+}. Above 0.2 wt% iron, the signals at 275 and 375 nm became dominant (Fig. 7, F), and they were clearly visible at 1 and 3 wt% iron (Fig. 7, G and H). Thus, at high Fe concentration, isolated octahedral Fe^{3+} and small Fe_xO_y clusters were formed in expense of tetrahedral (distorted) Fe^{3+}.

Fig. 8 shows the DRS spectra of FeO_x on silica promoted with different amounts of Rb sulfate compared with an unpromoted catalyst. The latter (Fig. 8, A) showed a maximum absorption around 255 nm with shoulders at 280 and 320 nm, indicative for (distorted) tetrahedral Fe^{3+}, octahedral Fe^{3+}, and small Fe_xO_y clusters. Up to Rb/Fe = 18 (Fig. 8, B–E), pro-

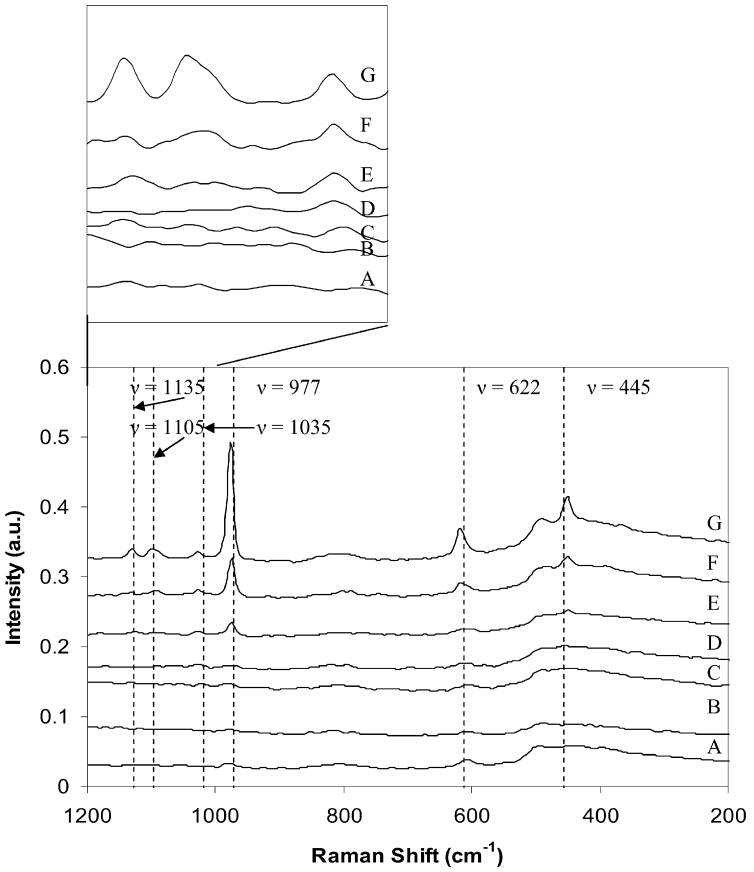

Fig. 6. Raman spectroscopy of promoted FeO_x on silica with different amounts of Rb_2SO_4. Catalyst: 0.1 wt% iron; Rb/Fe = 0 (A), 2.3 (B), 4.5 (C), 9 (D), 18 (E), 36 (F), and 72 (G). Insert: Raman shifts enlarged between 1150 and 1000 cm^{-1}.

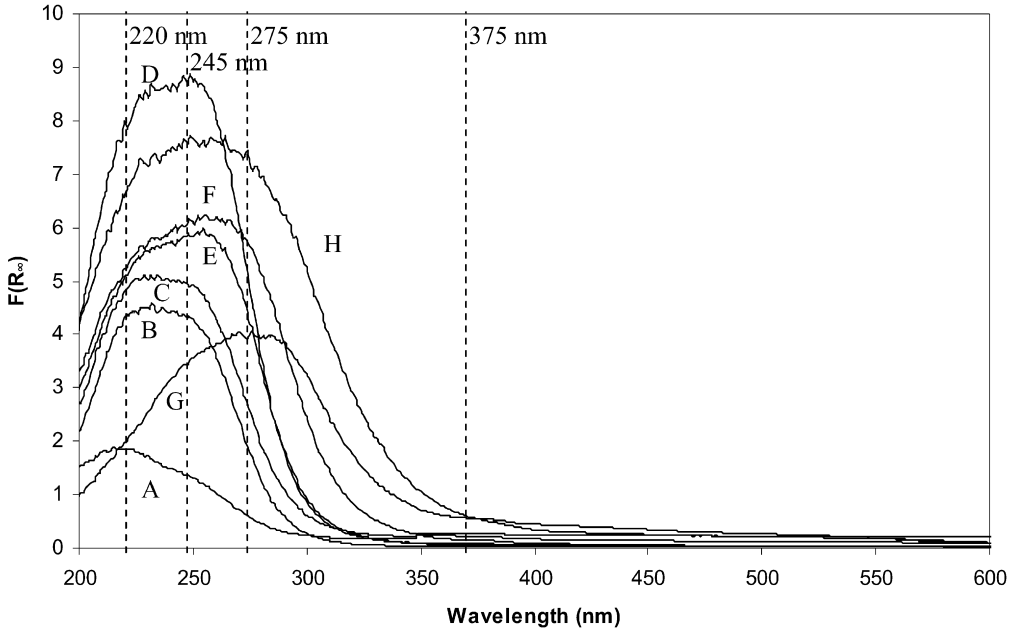

Fig. 7. UV–vis DRS spectra of Rb_2SO_4-promoted FeO_x on silica with different iron loadings, promoter/iron = 10. (A) 0 wt%, (B) 0.05 wt%, (C) 0.1 wt%, (D) 0.15 wt%, (E) 0.2 wt%, (F) 0.4 wt%, (G) 1 wt%, and (H) 3 wt% iron.

motion with Rb_2SO_4 clearly caused a blue shift to a relatively sharp absorption maximum around 245–255 nm in combination with a less obvious band at 230 nm, indicating the presence of tetrahedral Fe^{3+}. At higher Rb concentrations (Rb/Fe > 18; Fig. 8, F and G) the signal at 230 nm became dominant.

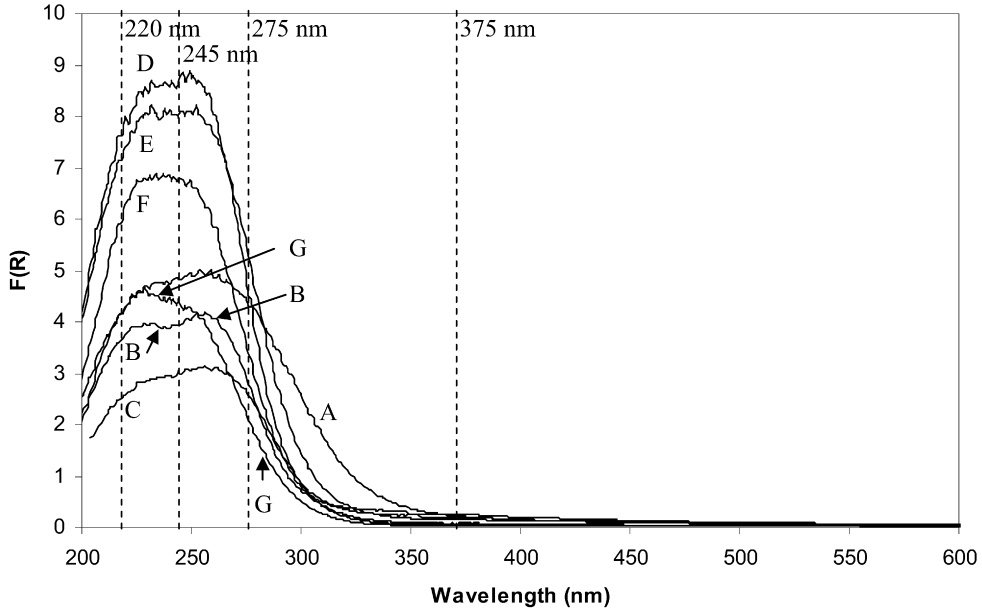

Fig. 8. UV–vis DRS spectra of promoted FeO_x on silica with different Rb_2SO_4 concentrations. Catalyst: 0.15 wt% iron; Rb/Fe = 0 (A), 2.3 (B), 4.5 (C), 12 (D), 18 (E), 36 (F), and 72 (G).

The use of different sulfate promoters influences the dispersion of iron (see Supplementary material, Fig. S5). Although all curves showed a maximum at 230–245 nm, corresponding to well-dispersed (distorted) tetrahedral Fe^{3+}, the major difference occurred at 300–450 nm, diagnostic of small iron oxide clusters. Absorption intensities were highest for Na and Li and lowest for Rb and K; thus, promotion with Rb_2SO_4 and K_2SO_4 produced the best iron oxide dispersion.

Kubelka–Munk transformation of the absorption data allows the calculation of absorption edge energies or band gap energies (E_g) [52–55], which give indirect information on the dispersion and coordination of Fe. The edge energies were extracted using the equation following Davis and Mott [56], $[F(R_\infty) \times h\nu] \sim (h\nu - E_g)^n$, with $n = 2$, 3, 1/2, and 3/2 according to the possible electron transitions. The best fit was obtained for $n = 2$ and $n = 1/2$, suggesting spin allowed, Laporte (or symmetry) partially forbidden (d–d) and spin allowed, Laporte allowed (LMCT) electron transitions from O^{2-} to Fe^{3+}, respectively. The edge energy values, derived from the x-intercept of the linearized low-energy region of $[F(R_\infty) \times h\nu]^{1/2}$ against $h\nu$, are collected in Table 7 (entries 1–8; Supplementary material, Fig. S6). An increase in Fe led to lower edge energies; an edge energy of 1.86 eV was found for pure Fe_2O_3 (Table 7, entry 9). Weber [53] and Gao and Wachs [55] proposed similar correlations between E_g and the average number of neighbors and local coordination structures in Mo^{6+} and V^{5+}, respectively. Accordingly, the decreased E_g with rising iron concentration indicates a transformation of isolated tetrahedral Fe^{3+} into isolated octahedral Fe^{3+} species and (tetrahedral or octahedral) species with increased nuclearity. When varying the concentration of Rb sulfate on the catalysts, the edge energy clearly rose with increasing Rb concentration (Table 7, entries 10–16) suggesting an evolution toward perfectly isolated Fe species.

Table 7
Edge energies in eV derived from the UV–vis DRS absorption spectra for Rb_2SO_4 (Rb/Fe = 10) promoted FeO_x on silica with different iron loadings

Entry	Fe concentration (wt%)	Fe concentration (atom/nm^2)	Edge energy (eV)[a]	Number of nearest neighbors, N_{Fe}[b]
1	0	0	4.21	0
2	0.05	0.011	4.23	0
3	0.1	0.022	4.14	0.25
4	0.15	0.032	4.15	0.22
5	0.2	0.043	4.06	0.56
6	0.4	0.086	3.85	1.36
7	1	0.22	3.58	2.41
8	3	0.65	3.58	2.40
9[c]	–	–	1.86	8.92
10[d]	0.15	0.032	3.94	1.01
11[e]	0.15	0.032	4.13	0.33
12[f]	0.15	0.032	4.12	0.34
13[g]	0.15	0.032	4.17	0.15
14[h]	0.15	0.032	4.22	0
15[i]	0.15	0.032	4.33	0
16[j]	0.15	0.032	4.34	0

[a] Edge energies are extracted by finding the intercept of the linearized low-energy region of a plot of $[F(R_\infty) \times h\nu]^{1/2}$ against $h\nu$, with $h\nu$ is the incident photon energy and $F(R_\infty)$ the Kubelka–Munk expression for DRS reflection.
[b] The average number of nearest Fe-neighbors is calculated using following empirical expression [49]: number of nearest Fe-neighbors $= 16 - 3.8 \times E_g$.
[c] Pure Fe_2O_3.
[d] Rb/Fe = 0.
[e] Rb/Fe = 2.25.
[f] Rb/Fe = 4.5.
[g] Rb/Fe = 12.
[h] Rb/Fe = 18.
[i] Rb/Fe = 36.
[j] Rb/Fe = 72.

3.4.7. EPR spectroscopy

EPR spectroscopy at X-band frequency was carried out to study the local environment and coordination geometry of the

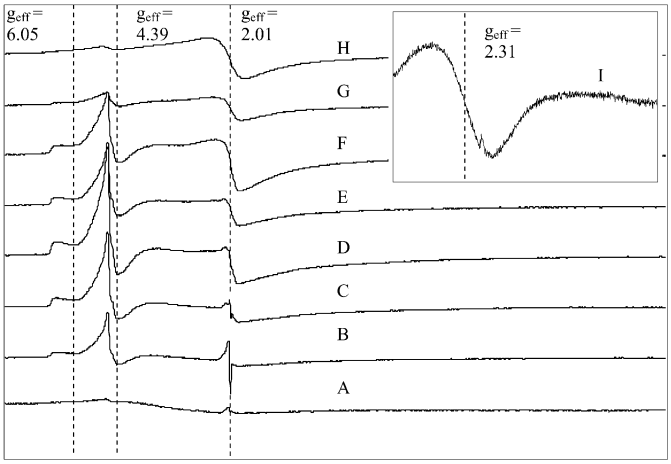

Fig. 9. X-band EPR spectra at 120 K of Rb_2SO_4-modified FeO_x on silica with different iron loadings at (A) 0 wt%, (B) 0.05 wt%, (C) 0.1 wt%, (D) 0.15 wt%, (E) 0.2 wt%, (F) 0.4 wt%, (G) 1 wt%, (H) 3 wt% iron, and (I) pure Fe_2O_3.

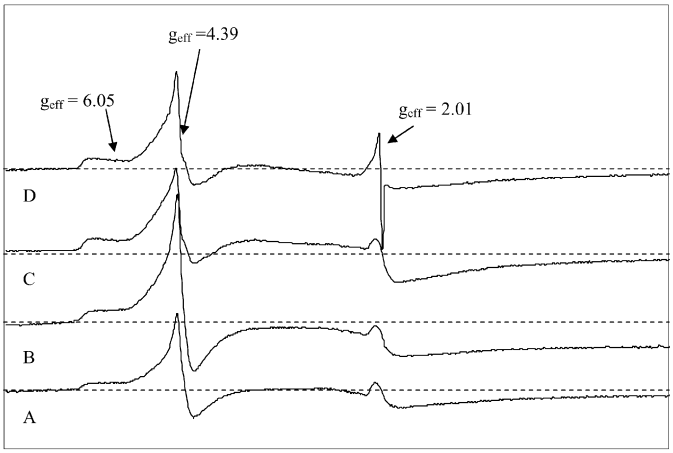

Fig. 10. X-band EPR spectra of unmodified and Rb_2SO_4-promoted FeO_x on silica at different temperatures. Catalyst: 0.05 wt% iron. (A) Unpromoted FeO_x on silica at 298 K, (B) unpromoted FeO_x on silica at 120 K, (C) Rb_2SO_4 (Rb/Fe = 12) modified FeO_x on silica at 298 K, and (D) Rb_2SO_4 (Rb/Fe = 12) modified FeO_x on silica at 120 K.

paramagnetic Fe(III) ions (with spin $S = 5/2$) of the Rb_2SO_4-promoted catalyst. The X-band spectra of the Fe catalyst with varying amounts of iron at 120 K are shown in Fig. 9. Fig. 10 shows the effect of temperature on the EPR transitions for an unpromoted and Rb_2SO_4-promoted 0.05 wt% FeO_x on silica.

Three signals can be distinguished in the spectra: $g_{eff} = 4.39$, accompanied by a shoulder at $g_{eff} = 6.05$ and a broad signal at $g_{eff} = 2.01$. As described in the literature [48,57], identification from the g_{eff} values only is not possible, because not only the coordination number, but also the local distortion of the Fe^{3+} ions influence the number and position of the EPR transitions. Only a simulation of the EPR spectrum by solving the spin Hamiltonian [57,58] with the appropriate zero field splitting parameters D and E will provide reliable information about the degree of distortion. Additional difficulties arise because the distortion can originate from either tetrahedral or octahedral Fe^{3+} [57,58]. Only after studying additional aspects, like the change of the EPR signals on dehydration [48,58], or by combining EPR with other characterization techniques like UV–vis DRS or Mössbauer [57], can unambiguous statements about the coordination be made. According to earlier work [18, 48,50,57,59–61], signals at $g_{eff} \sim 4.3$ and $g_{eff} \geqslant 6$ could be assigned to isolated Fe^{3+} in strong rhombic or axial distortion, respectively, irrespective of their coordination. Signals around $g_{eff} = 2$ can arise from isolated Fe^{3+} in high symmetry (sharp signal) or from Fe^{3+} in Fe_xO_y clusters (broadened signal). The Curie–Weiss law (intensity $\sim 1/T$) can be used to discriminate between these species.

As shown in Fig. 10, the transition around $g_{eff} \sim 2$ clearly reacted differently on cooling. For the unpromoted catalyst, cooling to 120 K left the signal around $g_{eff} \sim 2$ unchanged (a slight rise in the global intensity), while the signal at $g_{eff} = 4.39$ clearly rose. For the promoted catalyst, the signal intensity at $g_{eff} = 4.39$ also increased, whereas a sharp signal around $g_{eff} \sim 2$ became dominant. The broad signal at the same g_{eff} value clearly decreased on cooling. This behavior suggests that the region around $g_{eff} \sim 2$ of the spectrum comprised overlapping signals from different Fe^{3+} sites. The anti Curie–Weiss behavior of the broad part at $g_{eff} \sim 2$ suggests magnetic interaction between electron spins of neighboring Fe^{3+} ions caused alignment to the external magnetic field, resulting in increased intensity at higher temperatures. The temperature behavior indicates that the sharp transition at $g_{eff} = 2.01$ can be attributed to highly symmetric Fe^{3+}, whereas iron oxide clusters gave rise to the broad part of the signal at $g_{eff} = 2.01$. Comparison with the EPR spectrum of pure Fe_2O_3 (Fig. 9, I) allows us to make a tentative distinction between Fe^{3+} in large clusters (a new signal at $g_{eff} = 2.31$) and Fe^{3+} in small Fe_xO_y clusters ($g_{eff} = 2.01$).

The support signal (Fig. 9, A; $g_{eff} = 2.01$) resulted from small amounts of iron impurities in silica corresponding to perfectly symmetric framework Fe^{3+}, probably in tetrahedral coordination. On raising the amount of iron (Fig. 9, B–E) up to 0.2 wt%, the intensities of isolated iron signals ($g_{eff} = 6.05$, 4.39) increased, whereas the intensity of the Fe_xO_y signal ($g_{eff} = 2.01$, broad) remained constant. The signal of highly symmetric, isolated Fe^{3+} ($g_{eff} = 2.01$, sharp) slowly decreased in intensity when the iron concentration was increased from 0.05 to 0.2 wt%. A further rise in the iron concentration above 0.2 wt% iron led to a steep decrease of the signals at $g_{eff} = 6.05$, 4.39, and 2.01 in favor of a signal attributed to Fe_xO_y clusters; the sharp signal at $g_{eff} = 2.01$ completely disappeared at these Fe contents. In bulk iron oxide, only a signal at $g_{eff} = 2.31$ was found. In addition, the low intensities of the signals at 1 and 3 wt% iron were in agreement with spin–spin coupling in oxides, resulting in extinction of the signal. Note that the presence of EPR-invisible Fe^{2+} is less likely in our samples due to the strongly oxidizing conditions during synthesis and the thermal pretreatment under O_2 before the EPR measurement.

Variation of the Rb_2SO_4 concentration in the catalyst composition was also followed with EPR (see Supplementary material, Fig. S8). At low Rb concentrations (A and B), the signals of isolated Fe^{3+} were very weak, and the broad part of the signal at $g_{eff} = 2.01$ indicates the presence of small iron oxide clusters. On raising the amount of Rb (C, D, and E), the signals of distorted isolated iron became dominant, and the presence

of iron oxide clusters was minimized. Rubidium sulfate apparently helps keeping the sites isolated from each other.

4. Discussion

4.1. Choice of metal and promoter

As stated before, there is literature agreement on the necessity of iron oxide in propylene epoxidation with N_2O [32–37]. However, there is no agreement about the best promoting element and the exact role of the promoter. As such, we undertook an intensive screening of metals and promoters. Among the numerous metals tested, only iron was able to produce PO with high selectivity. Surprisingly, chromium showed activity toward propylene epoxidation. Because the epoxidation activity of chromium was much lower than that of iron, no further attention was given to this system.

Using iron oxide on silica and different acetate salts, the obtained catalytic results were in good agreement with some literature data [36,37], although in conflict with others advancing the use of KCl and CsAc [32–37]. Differences in preparation method, silica source, iron loading, and promoter/iron ratio likely influence the promoting effect of alkali metal salts. Screening of different alkali and earth alkali metal salt promoters showed that with our synthesis procedure, Rb_2SO_4 was the best promoter for FeO_x/silica.

4.2. Optimization of the catalyst's composition

Optimization of the composition revealed that a catalyst with 0.15 wt% FeO_x/silica, promoted with Rb_2SO_4 (with Rb/Fe $\sim$ 10) gave the best epoxidation results. Up to 0.15 wt% iron oxide, the activity per iron site remained constant (18 mmol PO $mmol^{-1}$ Fe h^{-1}), whereas higher iron concentrations (>0.2 wt% iron oxide) led to lower oxidation activity per iron. Metal clustering (Fe_xO_y), as evidenced by UV–vis DRS (shift to lower energy bands and lower edge energies) and EPR [decrease of (distorted) isolated FeO_x signals], resulted in deep oxidation. Thus, highly dispersed isolated iron oxide seems to be the active site that allows selective epoxidation.

The amount of promoter is crucial to achieving good PO selectivity; when the amount of Rb_2SO_4 is too low (Rb/Fe < 10), Fe dispersion is not optimal, resulting in low activity; moreover, the Brönsted acidity of the catalyst was not fully neutralized here, resulting in PO isomerization. Excess Rb_2SO_4 (Rb/Fe > 12) has no further beneficial effect on the activity and selectivity of the epoxidation, but forms a crystalline Rb_2SO_4 phase on the catalyst, as evidenced by XRD and Raman. At very high promoter loadings (Rb/Fe > 18), formation of basic Rb_2O from excess Rb_2SO_4 during catalyst pretreatment likely explains the slight activity decrease. Thus, a catalyst with Rb concentration of Rb/Fe = 10–12, having the highest concentration of distorted isolated iron oxide (from EPR) in tetrahedral coordination (from UV–vis), resulted in the highest PO yield.

4.3. Emphasis on the exact role of Rb_2SO_4

The use of different promoting salts (e.g., chloride, bromide, sulfate, and nitrate instead of acetate) influence the catalytic performance, in contrast to a literature claim that the anion in the promoter salt had no drastic effect [32–37]. We experienced a change in catalytic behavior using different anions (Na > K > Rb > Cs for acetates and Rb $\geqslant$ Cs > K > Na for sulfates), and clearly showed here that both cation and anion are crucial for an optimal promoting effect. We believe the effect of Rb_2SO_4 is dual; first, it has a structural effect on the catalyst by neutralizing surface acidity and facilitating the iron dispersion, with both Rb and sulfate playing roles. In addition, there is also evidence that it directly influences the activity of the catalyst, probably due to electronic effects (see further).

4.3.1. Neutralization of surface acidity

As suggested in the literature [32,36,37], the cationic part of the promoter salt neutralizes the surface acidity of the support. By combining the information of the IPA decomposition and the PO feed test, PO destabilization, and thus decreased PO selectivity, can be correlated with enhanced surface acidity. Consequently, there is the need for a promoter to neutralize the acidity. Indeed, fed PO is not stable in the presence of silica or FeO_x/silica in reaction conditions. On addition of Rb_2SO_4 this acidity almost fully disappears, leading to a much higher stability of PO.

4.3.2. Enhanced iron dispersion

Using a combination of UV–vis DRS and EPR spectroscopy, it became clear that the promoter has a second structural effect: influencing the Fe dispersion. Without Rb_2SO_4, iron forms mainly large Fe_xO_y clusters already at low Fe content, which are responsible for deep oxidation [62,63]. With Rb_2SO_4, probably due to competitive cation exchange between cationic Fe^{3+}-species and Rb^+, the formation of Fe_xO_y clusters diminishes in favor of (distorted) isolated iron oxide. The catalytic results indeed show that highly dispersed iron is required for selective epoxidation, and that the amount of cation is critical to achieving good iron dispersion. Besides the amount of cation, the cation's nature also affected the epoxidation results. Using different alkali metal sulfates as promoter results in following order of degree of Fe dispersion: Rb > Cs > K > Na > Li. Because this order matches that of the catalytic activity, we conclude that the epoxidation activity is governed by the metal dispersion, isolated iron oxide being the active site for epoxidation.

Importantly, one cannot exclude contribution of the anion to the improved dispersion; indeed, the presence of sulfate ligands between the iron sites might prevent direct Fe–O–Fe bridging. Raman experiments clearly show the presence of S=O vibrations in the promoted catalysts, indicating that sulfate is present on the catalyst. This is true for high Rb sulfate loadings (Rb/Fe > 12), where SO_4^{2-} appears as hexagonal Rb_2SO_4, whereas at low Rb concentrations, a distinct signal at 1035 cm^{-1} is visible indicative of iron(III)-sulfate. This bears a structural resemblance to iron phosphate structures reported

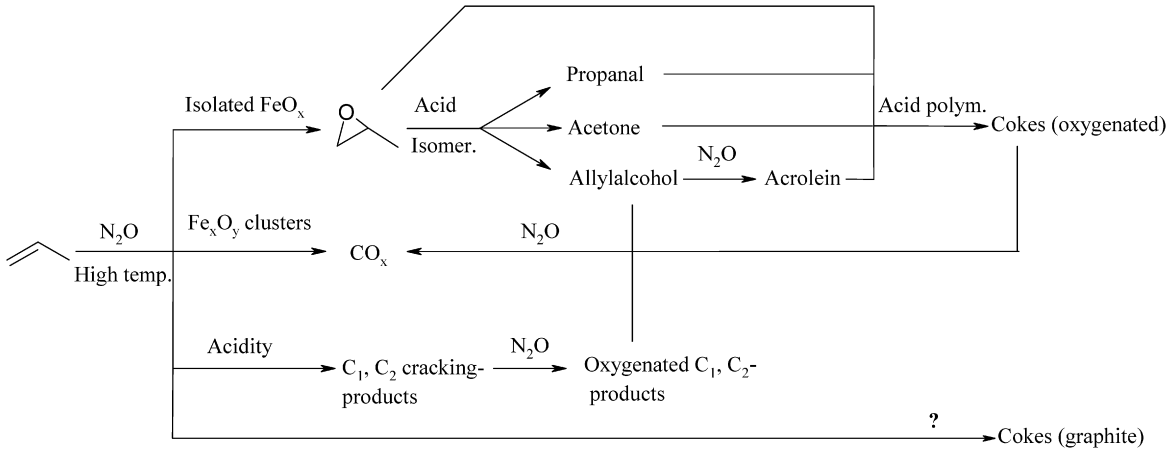

Fig. 11. Proposed reaction network for propylene epoxidation with N_2O and FeO_x catalyst.

for the selective oxidation of methane to methanol with N_2O [64,65]. Likewise, sulfate anions might form local structures in which the iron cations are captured, thus preventing iron clustering. As such, sulfate is involved in the dispersion of iron.

4.3.3. Electronic effect

High iron dispersions are also obtained using acetate promoters and not only by sulfate salts (see Supplementary material, Fig. S7). As Rb_2SO_4 is a better promoter than Rb acetate, other parameters besides iron dispersion influence the catalytic activity. In literature, sulfate is known to enhance the catalytic properties of vanadium catalysts in different oxidation reactions [66–72]. Some authors have proposed that sulfate in the vicinity of vanadyl sites electronically influences its redox properties, leading to enhanced catalytic performance [66]. Likewise, the presence of a sulfate ligand on an iron site, explaining the Raman signal at 1035 cm^{-1}, might influence the electronic configuration of iron and as such may explain the high activity of rubidium sulfate-promoted iron catalysts. Further research is ongoing to confirm this hypothesis.

4.4. Mechanistic proposal

As described in detail in the results section, PO selectivity is primarily governed by acid–base properties of the catalyst. In the absence of promoter, the relatively high acidity of the catalyst results in consecutive PO isomerization, yielding low PO selectivity; addition of promoter results in neutralization and high PO selectivity (>70%). The amount of iron has no major influence on PO selectivity; only at high iron concentration (>0.6 wt% iron or 0.13 Fe atoms per nm^2) are iron oxide clusters formed, which are responsible for deep oxidation.

Previous papers [33–35] addressed a selective allylic oxidation of propylene with N_2O over unpromoted FeO_x/silica. Using H_2-TPR, they observed that on modification with KCl, the reduction of Fe^{3+} to Fe^{2+} shifts to higher temperature [33]. The lower iron reducibility was explained by inhibition of the reactivity of lattice oxygen by the K^+ promoter. Their allylic oxidation is not entirely in line with our observations; in agreement with other papers [32,36,37], we observed the main formation of propanal (and a little acetone), whereas allylic oxidation products (such as allylic alcohol and acrolein) are formed only in minor quantities. Moreover, acrolein should not be seen as a primary product, because it can be formed from allylic alcohol. In light of the above observations (surface acidity and PO stability), we propose a reaction mechanism (Fig. 11) in which initially PO is the major reaction product. The epoxidation is catalyzed by isolated tetrahedral Fe^{3+} sites. The presence of Fe_xO_y clusters results in deep oxidation and formation of CO_x. Small amounts of CH_4, C_2H_4, and C_2H_6 and their oxygenated counterparts (methanol, ethanol, and acetaldehyde) could be explained by acid-cracking reactions of propylene, followed by oxidation. Due to acidity, PO isomerizes to propanal, acetone, and allyl alcohol, which can be further oxidized to acrolein. In addition, acid polymerization of secondary oxidation products might lead to polymer structures eventually lying at the origin of carbonaceous deposits, which deactivate the catalyst. Self-polymerization of PO to polyether compounds, as proposed by Ananieva and Reitzmann [32], also can contribute to deactivation. Analysis of the coke deposits should be easily made by IR spectroscopy, but unfortunately, the amount of deposits is too low to distinguish between both possibilities. XPS confirmed formation of carbon deposits on a spent catalyst; however, the binding energy of C was surprisingly not of oxygenated nature. Perhaps graphite-like coke is formed, independent from but dominant over the formation of oxygenated deposits. Further study is required to unravel the deactivation mechanism.

For future application, because the catalytic activity can easily be restored on burning the coke, one might think of integrating state-of-the-art continuous (as in FCC) or discontinuous (with two reactor units) regeneration technologies.

5. Conclusion

The gas-phase epoxidation of propylene using N_2O as an oxidant was studied to screen for an ideal catalyst composition. Only catalysts containing iron (and to some extent chromium) oxide on silica show selective PO production when modified with alkali and earth alkali salts. Using various promoters, it became evident that both anion and cation are crucial for the

epoxidation activity and PO selectivity, and that Rb sulfate is the modifier of choice. Variation of the amount of modifier and Fe led to an optimal composition of 0.15 wt% Fe and Rb_2SO_4 (Rb/Fe = 12). This particular catalyst results in a propylene conversion of 16.8% and a PO selectivity of 59% after 80 min of reaction. As further raising the iron concentration leads to Fe_xO_y formation and deep oxidation of propylene, only highly dispersed iron oxide is capable of producing PO. This is confirmed by UV–vis DRS and EPR spectroscopy, suggesting the active iron site has a distorted tetrahedral coordination. Raman spectroscopy suggests the presence of sulfate in the vicinity of iron, enhancing its redox properties. The promoter also plays a structural role. Besides better iron dispersion, the promoter also neutralizes acid sites, preventing consecutive reactions with the formed PO. A mechanism for propylene epoxidation with N_2O is proposed based on acidity and PO stability experiments, and suggests PO as the major primary product.

Because Rb_2SO_4-promoted FeO_x/silica is the most promising catalyst combination, we have undertaken an extensive physicochemical characterization study using additional techniques (e.g., EXAFS, pulsed EPR, probe FT-IR, Mössbauer, H_2-TPR, magnetic circular dichroism and magnetization measurements [73]) in an attempt to gain insight into the active iron site and better understand the fundamentals of the catalyst deactivation.

Acknowledgments

This work was supported by CECAT (Centre of Excellence, Leuven University), IDECAT (European Centre of Excellence Network), IAP, and GOA. The authors thank Kevin Huyghe for assistance with the practical work. V. Meynen is grateful to the FW-Flanders for financial support. Inside Pores (European Centre of Excellence Network) is also acknowledged.

Supplementary material

The online version of this article contains additional supplementary material.

Please visit DOI:10.1016/j.jcat.2007.01.001.

References

[1] T. Levander, Atmos. Environ. Part A Gen. Top. 24 (1990) 2707.
[2] W.C. Togler, Coord. Chem. Rev. 187 (1999) 303.
[3] J. Jia, K.S. Pillai, W.M.H. Sachtler, J. Catal. 221 (2004) 119.
[4] A. Waclaw, K. Nowinska, W. Schwieger, Appl. Catal. A 270 (2004) 151.
[5] Q. Zhu, R.M. van Teeffelen, R.A. van Santen, E.J.M. Hensen, J. Catal. 221 (2004) 575.
[6] L. Capek, P. Kubanek, B. Wichterlova, Z. Sobalik, Collect. Czech. Chem. Commun. 68 (2003) 1805.
[7] E.J.M. Hensen, Q. Zhu, R.A. Van Santen, J. Catal. 220 (2003) 260.
[8] D.P. Ivanov, V.I. Sobolev, G.I. Panov, Appl. Catal. A 241 (2003) 113.
[9] A.A. Ivanov, V.S. Chernyavsky, M.J. Gross, A.S. Kharitonov, A.K. Uriarte, G.I. Panov, Appl. Catal. A 249 (2003) 327.
[10] D. Meloni, R. Monaci, V. Solinas, G. Berlier, S. Bordiga, I. Rossetti, C. Oliva, L. Forni, J. Catal. 214 (2003) 169.
[11] K. Yoshizawa, Y. Shiota, T. Kamachi, J. Phys. Chem. B 107 (2003) 11404.
[12] B. Louis, P. Reuse, L. Kiwi-Minsker, A. Renken, Appl. Catal. A 210 (2001) 103.
[13] L.M. Kustov, A.L. Tarasov, V.I. Bogdan, A.A. Tyrlov, J.W. Fulmer, Catal. Today 61 (2000) 123.
[14] A. Ribera, I.W.C.E. Arends, S. de Vries, J. Perez-Ramirez, R.A. Sheldon, J. Catal. 195 (2000) 287.
[15] V.I. Sobolev, K.A. Dubkov, E.A. Paukshtis, L.V. Pirutko, M.A. Rodkin, A.S. Kharitonov, G.I. Panov, Appl. Catal. A 141 (1996) 185.
[16] V.I. Sobolev, A.S. Kharitonov, Ye.A. Paukshtis, G.I. Panov, J. Mol. Catal. 84 (1993) 117.
[17] A. Reitzmann, E. Klemm, G. Emig, Chem. Eng. J. 90 (2002) 149.
[18] P. Kubanek, B. Wichterlova, Z. Sobalik, J. Catal. 211 (2002) 109.
[19] V.N. Parmon, G.I. Panov, A. Uriarte, A.S. Noskov, Catal. Today 100 (2005) 115.
[20] B.R. Wood, J.A. Reimer, A.T. Bell, M.T. Janicke, K.C. Ott, J. Catal. 225 (2004) 300.
[21] K.A. Dubkov, V.I. Sobolev, G.I. Panov, Kinet. Catal. 39 (1998) 72.
[22] N.S. Ovanyesan, A.A. Shteinman, K.A. Dubkov, V.I. Sobolev, G.I. Panov, Kinet. Catal. 39 (1998) 792.
[23] G.I. Panov, V.I. Sobolev, K.A. Dubkov, A.E. Parmon, N.S. Ovanyesan, A.E. Shilov, A.A. Shteinman, React. Kinet. Catal. Lett. 61 (1997) 251.
[24] E.V. Kondratenko, J. Pérez-Ramirez, Appl. Catal. A 267 (2004) 181.
[25] R. Bulanek, B. Wichterlova, K. Novoveska, V. Kreibich, Appl. Catal. A 264 (2004) 13.
[26] E.V. Kondratenko, M. Baerns, Appl. Catal. A 222 (2001) 133.
[27] S.S. Hong, J.B. Moffat, Appl. Catal. A 109 (1994) 117.
[28] M.B. Ward, M.J. Lin, J.H. Lunsford, J. Catal. 50 (1977) 306.
[29] E.V. Kondratenko, M. Cherian, M. Baerns, Catal. Today 112 (2006) 60.
[30] M.H. Groothaert, P.J. Smeets, B.F. Sels, P.A. Jacobs, R.A. Schoonheydt, J. Am. Chem. Soc. 127 (2005) 1394.
[31] G. Ondrey, Chem. Eng. (New York) 111 (9) (2004) 17.
[32] E. Ananieva, A. Reitzmann, Chem. Eng. Sci. 59 (2004) 5509.
[33] X. Wang, Q. Zhang, Q. Guo, Y. Lou, L. Yang, Y. Wang, Chem. Commun. 12 (2004) 1396.
[34] X. Wang, Q. Zhang, S. Yang, Y. Wang, J. Phys. Chem. B 109 (2005) 23500.
[35] Q. Zhang, Q. Guo, X. Wang, T. Shishido, Y. Wang, J. Catal. 239 (2006) 105.
[36] D. Hönicke, V. Duma, W. Krysmann (Creavis Gesellschaft fuer Technologie und Innovation mbH), US Patent 6392065 (2002).
[37] Duma, D. Hönicke, J. Catal. 191 (2000) 93.
[38] D.L. Trent (The Dow Chemical Company), Kirk Othmer Encyclopedia Chem. Technol. 20 (1996) 271.
[39] A. Gervasini, A. Auroux, J. Catal. 131 (1991) 190.
[40] Powder Diffraction File, Alphabetical Indexes, Inorganic Phases Sets 1–45, ICDD, 1995.
[41] D. Liu, H.M. Lu, J.R. Hardy, Phys. Rev. B 44 (1991) 7387–7393.
[42] Y.I. Yuzyuk, V.I. Torgashev, R. Farhi, I. Gregora, J. Petzelt, P. Simon, D. De Sousa Meneses, L.M. Rabkin, J. Phys. Condens. Matter 10 (1998) 1157–1173.
[43] S. Bordiga, R. Buzzoni, F. Geobaldo, C. Lamberti, E. Giamello, A. Zecchina, G. Leofanti, G. Petrini, G. Tozzola, G. Vlaic, J. Catal. 158 (1996) 486.
[44] A.B.P. Lever, Inorganic Electronic Spectroscopy, Studies in Physical and Theoretical Chemistry, vol. 33, second ed., Elsevier, 1984, pp. 452–453 and 161–173.
[45] G. Centi, S. Perathoner, R. Arrigo, G. Giordano, A. Katovic, V. Pedula, Appl. Catal. A 307 (2006) 30.
[46] G. Centi, S. Perathoner, F. Pino, R. Arrigo, G. Giordano, A. Katovic, V. Pedula, Catal. Today 110 (2005) 211.
[47] F. Arena, G. Gatti, G. Martra, S. Coluccia, L. Stievano, L. Spadaro, P. Famulari, A. Parmaliana, J. Catal. 231 (2005) 365.
[48] M.S. Kumar, M. Schwidder, W. Grünert, A. Brückner, J. Catal. 227 (2004) 384.
[49] C. Nozaki, C.G. Lugmair, A.T. Bell, T. Don Tilley, J. Am. Chem. Soc. 124 (2002) 13194.
[50] V. Umamaheswari, W. Böhlmann, A. Pöppl, A. Vinu, M. Hartmann, Micropor. Mesopor. Mater. 89 (2006) 47.
[51] N. Maxim, A. Overweg, P.J. Kooyman, J.H.M.C. van Wolput, R.W.J.M. Hanssen, R.A. van Santen, H.C.L. Abbenhuis, J. Phys. Chem. B 106 (2002) 2203.

[52] Q. Zhang, Q. Guo, X. Wang, T. Shishido, Y. Wang, J. Catal. 239 (2006) 105.
[53] R.S. Weber, J. Catal. 151 (1995) 470.
[54] X. Gao, S.R. Bare, B.M. Weckhuysen, I.E. Wachs, J. Phys. Chem. B 102 (1998) 10842.
[55] X. Gao, I.E. Wachs, J. Phys. Chem. B 104 (2000) 1261.
[56] E.A. Davis, N.F. Mott, Philos. Mag. 22 (1970) 903.
[57] B.M. Weckhuysen, In-Situ Spectroscopy of Catalysts, American Scientific Publishers, Stevenson Ranch, CA, 2004, pp. 220–222 and 240–243.
[58] D. Goldfarb, M. Bernardo, K.G. Strohmaier, D.E.W. Vaughan, H. Thomann, J. Am. Chem. Soc. 116 (1994) 6344.
[59] A.M. Ferretti, C. Oliva, L. Forni, G. Berlier, A. Zecchina, C. Lamberti, J. Catal. 208 (2002) 83.
[60] H. Guo, X. Zhang, M. Cui, R. Sharma, N. Yang, D.L. Akins, Mater. Res. Bull. 40 (2005) 1713.
[61] P. Selvam, S.E. Dapurkar, S.K. Badamali, M. Murugasan, H. Kuwano, Catal. Today 68 (2001) 69.
[62] F. Arena, G. Gatti, G. Martra, S. Coluccia, L. Stievano, L. Spadaro, P. Famulari, A. Parmaliana, J. Catal. 231 (2005) 365–380.
[63] A. Parmaliana, F. Arena, J. Catal. 167 (1997) 57–65.
[64] Y. Wang, K. Otsuka, J. Mol. Catal. A Chem. 111 (1996) 341.
[65] A.V. Annapragada, E. Gulari, J. Catal. 123 (1990) 130.
[66] E. Garcia-Bordejé, J.L. Pinilla, M.J. Lazaro, R. Moliner, J.L.G. Fierro, J. Catal. 233 (2005) 166–175.
[67] A. Martin, U. Bentrup, G.U. Wolf, Appl. Catal. A Gen. 227 (2002) 131–142.
[68] D. Klissurski, N. Abadzhijeva, React. Kinet. Catal. Lett. 2 (1975) 431–438.
[69] U. Bentrup, A. Martin, G.U. Wolf, Catal. Today 78 (2003) 229–236.
[70] D. Monti, A. Reller, A. Baiker, J. Catal. 93 (1985) 360–367.
[71] D.W.B. Westerman, N.R. Foster, M.S. Wainwright, Appl. Catal. 3 (1982) 151–160.
[72] N.R. Foster, M.S. Wainwright, D.W.B. Westerman, Aust. J. Chem. 34 (1981) 1325–1330.
[73] G.D. Pirngruber, P.K. Roy, R. Prins, Phys. Chem. Chem. Phys. 8 (2006) 3939–3950.